Effect of Interlayer Coupling on Ultrafast Charge Transfer from Semiconducting Molecules to Mono- and Bilayer Graphene

Ti Wang,[1,*] Qingfeng Liu,[1] Claudiu Caraiani,[1] Yupeng Zhang,[2] Judy Wu,[1] and Wai-Lun Chan[1,†]

[1]*Department of Physics and Astronomy, University of Kansas, Lawrence, Kansas 66045, USA*

[2]*Department of Materials Science and Engineering, Monash University, Clayton 3800, Victoria, Australia*

(Received 25 February 2015; revised manuscript received 12 April 2015; published 24 July 2015)

Graphene is used as flexible electrodes in various optoelectronic devices. In these applications, ultrafast charge transfer from semiconducting light absorbers to graphene can impact the overall device performance. Here, we propose a mechanism in which the charge-transfer rate can be controlled by varying the number of graphene layers and their stacking. Using an organic semiconducting molecule as a light absorber, the charge-transfer rate to graphene is measured by using time-resolved photoemission spectroscopy. Compared to graphite, the charge transfer to monolayer graphene is about 2 times slower. Surprisingly, the charge transfer to *A*-*B*–stacked bilayer graphene is slower than that to both monolayer graphene and graphite. This anomalous behavior disappears when the two graphene layers are randomly stacked. The observation is explained by a charge-transfer model that accounts for the band-structure difference in mono- and bilayer graphene, which predicts that the charge-transfer rate depends non-intuitively on both the layer number and stacking of graphene.

DOI: 10.1103/PhysRevApplied.4.014016

I. INTRODUCTION

Graphene and related two-dimensional (2D) crystals are promising candidates for materials used in next-generation optoelectronic devices [1–6]. In organic devices such as photovoltaics [7–10], photodetectors [11,12], and light-emitting diodes [13,14], single-layer and few-layer graphene have replaced the commonly used indium tin oxide as the conducting electrode because of its superior mechanical, electronic, and optical properties. Previous works focus on balancing the transparency and the sheet resistance of graphene by varying the layer number [15] or on controlling the electronic properties by molecular doping (ground-state charge transfer) [16,17]. However, dynamic processes such as the transfer of localized charges from organic materials to graphene are less explored [18–20]. An interesting question is whether the charge-transfer (CT) rate depends on the number of graphene layers and the stacking. The stacking of van der Waals layers, in principle, affects the band structure of graphene and the electronic coupling between graphene and the light absorber, but its effect on CT is not known. Indeed, the ability to tune the layer number and stacking in 2D materials has offered many exciting opportunities in controlling properties such as energy (exciton) transfer rate [21], nonlinear optical susceptibility [22,23], and proton permeability [24]. In some cases, changing the stacking can also lead to the formation of new electronic phases [25,26].

In this work, we use time-resolved two-photon photoemission spectroscopy (TR 2PPE) and ultraviolet photoemission spectroscopy (UPS) to study the CT rate and the electronic structure of the interface formed between a commonly used organic semiconductor, zinc phthalocyaine (ZnPc), and graphene. Compared to bulk substrates such as graphite and Au, CT to graphene is found to be about 2–4 times slower, which can be attributed to the low density of state (DOS) of graphene near the Fermi level. Surprisingly, CT to *AB*-stacked bilayer graphene (BG) is slower than that to both single-layer graphene (SG) and graphite. Furthermore, the slower CT rate is not observed in the randomly stacked BG. This nontrivial behavior can be explained by the change in the electronic band structure of graphene induced by the electronic coupling between the two graphene layers, which in turn affects the electronic coupling between graphene and the organic molecule. Based on this result, we predict that the CT rate can be controlled by varying the number of layers and stacking of graphene.

II. EXPERIMENTS

Large area SG and *AB*-stacked BG are deposited on Si wafers covered with 90 nm-thick thermal oxide *directly* by using chemical vapor deposition (CVD). This method avoids surface contaminations commonly found in transferred graphene. A clean SiO_2 on Si substrate is placed at the center of a quartz tube reactor inside a horizontal CVD furnace. The growth conditions for SG are 140 sccm H_2 flow, 20 sccm CH_4 flow, and a growth temperature of 1100 °C; whereas the growth conditions for BG are

*Corresponding author.
wangti@ku.edu
†Corresponding author.
wlchan@ku.edu

 © 2015 American Physical Society

120 sccm H_2 flow, 30 sccm CH_4 flow, and a growth temperature of 1090 °C. Raman spectroscopy is used to characterize graphene samples, which can provide information such as the number of layers and stacking order [27–30]. Figure 1 shows typical Raman spectra of the as-synthesized SG and BG sample. In the Raman spectra, three characteristic peaks, i.e., 2D band, *G* band, and *D* band, can be identified. The ratio of the 2D band to the *G*-band intensity (I_{2D}/I_G) is 2.6 and 1.1 for SG and BG, respectively, which are the ratios commonly observed for monolayer and *AB*-stacked bilayer graphene [31–33]. The intensity ratio of *D* to *G* band, which correlates to the defect density, is 0.25 (0.26) for SG (BG). This ratio is small compared to that commonly observed in CVD graphene. The graphene is homogenous with over 95% coverage as determined by Raman mapping [34]. The optical and atomic force microscopy images of the samples, which are shown in Ref. [35], indicate that the graphene is uniform and continuous. The work function of the graphene determined by UPS is 4.5 eV, which is similar to that of pristine graphene (4.5–4.6 eV) [36], implying a very low doping level. Unless otherwise stated, experiments on graphene are done with samples grown directly on SiO_2.

Randomly stacked BG samples are used in one of the control experiments. These samples are prepared by transferring two single-layer graphene grown on Cu successively to the SiO_2 on Si substrate by using the standard solution method [37]. In this case, the two graphene layers do not have a defined stacking relationship. Similar to the direct-grown single-layer graphene, the transferred SG has a I_{2D}/I_G ratio larger than 2, which is a characteristic feature of monolayer graphene. The transferred graphene has a less pronounced *D* peak. It is known that graphene grown on Cu has a lower defect density compared to graphene grown on SiO_2, which results in the very weak *D*-peak intensity. Furthermore, the ratio of the 2D band to the *G*-band intensity for the transferred BG [Fig. 1(b)] is approximately 2.1. *AB*-stacked BG should have $I_{2D}/I_G \approx 1$ [Fig. 1(a)], while SG should have $I_{2D}/I_G > 2$. The larger ratio found in transferred BG indicates that the two graphene layers in the randomly stacked sample are not coupled to each other. This agrees with a previous finding in which the band structure of single-layer graphene is preserved in misoriented few-layer graphene [38].

ZnPc molecules (Luminescence Technology, >99%), which are served as light absorbers, are deposited on SG, BG, highly ordered pyrolytic graphite (HOPG), Au, and SiO_2 substrates by thermal evaporation in an ultrahigh vacuum chamber (UHV) with base pressure $<5 \times 10^{-10}$ Torr. For the HOPG sample, a fresh surface is formed by cleaving the substrate with scotch tape before the sample is introduced into the UHV chamber. For SG, BG, HOPG, and SiO_2 substrates, the sample is annealed for 12–24 h in the UHV chamber before deposition. The Au (111) surface is prepared by standard sputtering and annealing cycles. The ZnPc molecules are deposited on different substrates at room temperature at a rate about 0.8–1 Å/ min, and the film thickness is measured by a quartz-crystal microbalance. After deposition, the sample is transferred under the UHV environment to another chamber with a base pressure $<1 \times 10^{-10}$ Torr, where UPS and 2PPE experiments are performed. On all substrates, the ZnPc molecules have a face-on orientation as determined by the work function of the samples [35].

Photoemission experiments are done both at room temperature and at 150 K. The sample is excited by a visible pump laser pulse with photon energy ($h\nu_1$) centered at 1.75 eV, which is chosen to match the exciton absorption peak of ZnPc crystals. The pulses (energy about 280 nJ and duration about 25 fs) are generated by a noncollinear optical parametric amplifier (NOPA) (Orpheus-N-2H, Light Conversion). The excited electrons are ionized by a time-delayed probe pulse ($h\nu_2 = 4.43$ eV, pulse energy about 5 nJ, and pulse duration about 55 fs), which is frequency doubled from the output of another NOPA (Orpheus-N-3H, Light Conversion). The probe photon energy is chosen to be around the sample work function to avoid one-photon photoemission. Both NOPAs are pumped by a Yb:KGW regenerative amplifier running at 125 kHz (Pharos 10 W, Light Conversion). The full width at half maximum (FWHM) beam diameter at the sample is 0.8 mm. The photoelectrons are detected by a hemispherical electron-energy analyzer (Phoibos 100, SPECS).

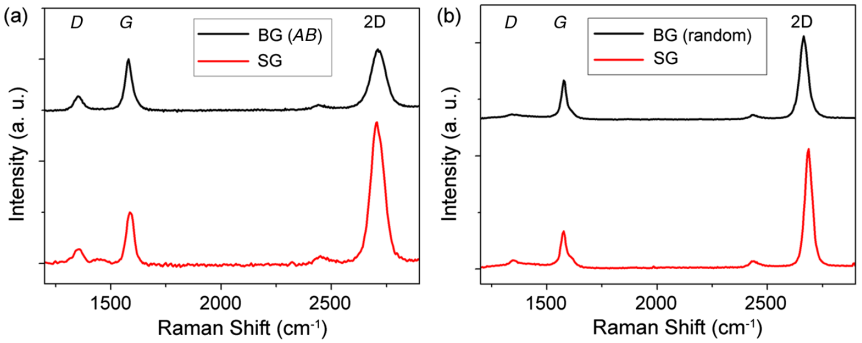

FIG. 1 (a) Raman spectra of SG and *AB*-stacked BG directly grown on SiO_2/Si substrates. (b) Raman spectra of the transferred SG and BG samples. For the BG sample, the two layers are transferred successively and have a random-stacking relationship.

III. RESULTS

A. Energy-level alignment at the interface

Since CT can be sensitive to the band alignment at the interface, the energetic positions of ZnPc unoccupied states with respect to the substrate's Fermi level (E_F) are first determined. Figure 2(a) shows the UPS spectra (spectra below E_F) together with the 2PPE spectra (spectra above E_F) for samples with 0.5 nm of ZnPc deposited on various substrates. The position of the highest occupied molecular orbital (HOMO) of ZnPc can be determined from the UPS spectra on the left. The 2PPE spectra can be used to determine energetic positions of the excited states. In Fig. 2(b), 2PPE spectra at a delay time equal to 100 fs are shown on the right. In order to show the intermediate states excited by the pump pulse exclusively, all the 2PPE spectra presented are subtracted by the corresponding background spectrum obtained at negative delay times. A typical time-resolved spectrum for the ZnPc/SG sample before background subtraction is shown in Ref. [35].

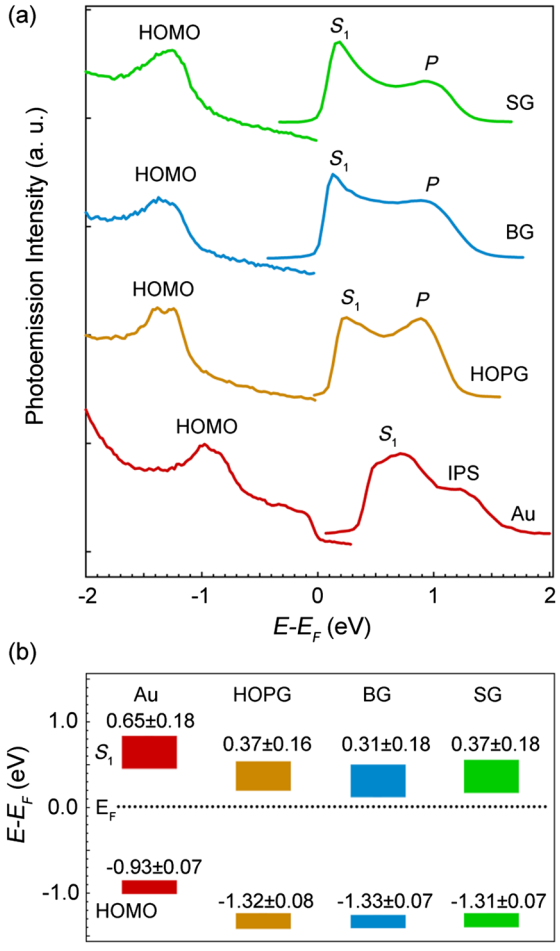

FIG. 2 Energy-level alignment at the interface. (a) UPS (left) and 2PPE (right) spectra for 0.5 nm ZnPc films deposited on various surfaces, which show the occupied and unoccupied band structures, respectively. The energy is referenced with respect to the Fermi level E_F. (SG, single-layer graphene; BG, bilayer graphene; HOPG, graphite; and Au, gold.) (b) The alignment of the HOMO (bottom) and S_1 state (top) of ZnPc with respect to E_F. The unit for the numbers is eV.

For the SG, BG, and HOPG samples, two peaks can be identified. The lower energy peak is located at around 1.6–1.7 eV above the HOMO peak of ZnPc. Since the energy separation from the HOMO to this peak matches the lowest absorption peak of ZnPc crystals, we have previously assigned it to the optically excited singlet exciton (S_1) in ZnPc [39]. The S_1 peak persists for thicker (10-nm) ZnPc samples [39]. Another peak, which is labeled as "*P*," is located at a higher energy. This peak is short-lived (lifetimes approximately 65–80 fs) and is related to the interface because its intensity diminishes with increasing ZnPc thickness. The energy of this state (2.2–2.4 eV above the HOMO peak) is too high to be excited directly from the HOMO with our pump pulse (1.75 eV). Therefore, we propose that this state is originated from electrons optically excited from the substrate to the lowest unoccupied molecular orbital (LUMO) of ZnPc. The approximately 0.7-eV separation between the S_1 and *P* peak can be accounted for by the exciton binding energy. A similar peak assignment has been made for α-sexithiophene, in which the exciton peak is located at approximately 0.9 eV below the LUMO peak [40]. The position of this state is also consistent with previous inverse photoemission measurements in which the bottom of the LUMO band is found to be about 2.4 eV above the HOMO peak [41]. Another possible origin for the *P* peak can be an interfacial state similar to those observed in metal-organic interfaces [42,43]. For the ZnPc molecules deposited on Au, both the HOMO and S_1 are located at higher energies with respect to E_F, but the separation between the two is consistent with the optical band gap of ZnPc. In ZnPc on Au, an additional state called the image potential state (IPS) can be identified. The IPS is distinct from other peaks in the time-resolved spectrum, since it has a negative lifetime (it is pumped by the UV pulse and probed by the visible pulse). The IPS has been studied previously [44,45] and is outside the scope of this work. In this work, we will focus on the S_1 state.

Figure 1(b) shows the energetic alignment of the S_1 state with respect to E_F for all substrates. The height of the boxes represents the width of the peaks observed in the spectra. Except for films deposited on Au, all samples have a similar energetic alignment in which the S_1 state is located at 0.3–0.4 eV above E_F. Furthermore, in both BG and SG, there is no significant shift (<0.02 eV) in the position of the graphene σ band with respect to E_F after ZnPc deposition [35], implying that the graphene is not significantly doped by ZnPc. For comparison, previous work finds that, when FePc is deposited on graphene, ground-state charge transfer from FePc to graphene causes the Fermi level to shift up only by 0.08 eV [46]. The doping effect of ZnPc is expected

to be even less due to the much weaker molecule-substrate interaction compared to that of FePc [47].

B. Ultrafast charge-transfer dynamics

In order to determine the CT rate, time-resolved spectra for a thick ZnPc film (10 nm) and an ultrathin ZnPc film (0.5 nm) deposited on the same substrate are compared. In general, because the photoemission probe is surface sensitive, only the very top layer (approximately 1–2 nm [48]) of the sample is probed. As a result, the CT dynamics can be probed from a thin ZnPc sample, while the intrinsic dynamics of the ZnPc film can be determined from a thick ZnPc sample. We have demonstrated previously that 2PPE can be a sensitive probe for CT [39,49,50]. More importantly, in our current case, all the substrates used have a band gap near the Γ point (the region in k space that is measured in our experiment). As a result, the 2PPE signal contributed by the substrates is expected to be weak. For example, in graphene, the Dirac cone is located at the K point in k space. Direct photoionization of excited electrons in the Dirac cone with our approximately 4.5-eV photons is forbidden, because the parallel momentum of electrons cannot be conserved during photoemission [51]. A much higher photon energy (>16 eV) is needed to directly ionize the hot electrons in graphene [52]. In our experiment, the hot electrons in the Dirac cone of graphene cannot be directly ionized. As a result, the photoemission signal observed for the bare graphene is nearly an order of magnitude weaker than that for the 0.5 nm ZnPc on graphene sample (Fig. S7 in Ref. [35]). Note that the large increase in signal after ZnPc deposition cannot be explained by the increase in optical absorption. This is because single-layer graphene is a stronger light absorber compared to the 0.5-nm-thick ZnPc [35]. The weak 2PPE signal from bare graphene is also consistent with previous measurements done with graphene on single-crystal metals in which only the IPS is observed [53]. Therefore, we can safely assume that the 2PPE signal from the ultrathin ZnPc samples is mainly originated from the ZnPc molecules. Similarly, a weak 2PPE signal is observed for other bare substrates used in this study.

Figures 3(a) and 3(b) show the TR-2PPE spectra for ZnPc deposited on SG. The color scale represents the photoemission intensity, which is proportional to the population of the excited states. For the 0.5-nm film, the lifetime of the S_1 exciton is very short (time constant about 100 fs). The observed lifetime agrees with the time scale commonly found for CT in organic semiconductors [54,55], inorganic materials [56,57], and hybrid interfaces [58] but is at least an order of magnitude smaller than the typical energy-transfer time [59]. In contrast, for the 10-nm sample [Fig. 3(b)], the rate of intensity decay for the S_1 peak is orders of magnitude slower, and the majority of the signal decays with a time constant on the order of 10–100 ps. At this thickness, the exciton near the surface cannot interact directly with the substrate, and the dynamics within the time window considered is insensitive to the film thickness [39]. Hence, the dynamics for the 10-nm sample represents the intrinsic dynamics of the ZnPc film. On the other hand, the ultrafast signal decay observed in the 0.5-nm film is not originated from the intrinsic dynamics of ZnPc. We attribute it to CT from the S_1 state to graphene. To further confirm that the ultrafast signal decay is mainly contributed by CT, an ultrathin layer of ZnPc is deposited on Si covered with native oxide in which no CT is expected. In this case, no rapid intensity decay is observed, and the dynamics is similar to that of a 10-nm film [Figs. 4(a) and 4(b)]. The time-resolved spectra for ZnPc on BG, HOPG, and Au are qualitatively similar [35]. For the 0.5-nm samples, the intensity decreases with a time constant that depends on the substrate due to different CT rates.

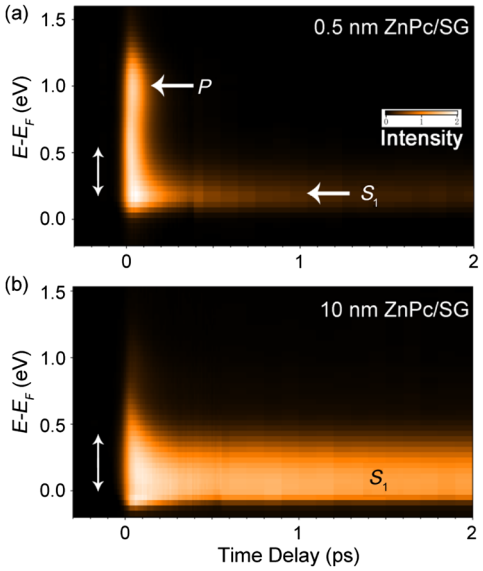

FIG. 3 Time-resolved photoemission spectrum for ZnPc on single-layer graphene showing ultrafast electron transfer. (a) 0.5 nm ZnPc on SG and (b) 10 nm ZnPc on SG. The color scale represents the photoemission intensity which is proportional to the excited state population. The rapid intensity decay for the S_1 peak for the 0.5-nm sample is due to electron transfer from ZnPc to graphene.

In Fig. 3(a), the intensity of the higher-energy portion of the S_1 peak decreases at a faster rate compared to that of the lower-energy portion of the peak, which causes narrowing of the S_1 peak. This can be explained by faster CT for electrons with more excess energy. To determine the average CT rate, the intensity is integrated over an energy range as shown by the vertical arrow in Fig. 3. The integrated intensity as a function of time is shown in Fig. 4(a). The initial intensity drop is fitted with an exponential decay convoluted with the finite width of the laser pulses (solid lines). The inverse of the CT rate for SG, BG, HOPG, and Au samples is 140 ± 20, 190 ± 20, 70, and 37 fs, respectively. For comparison, CT from similar organic molecules

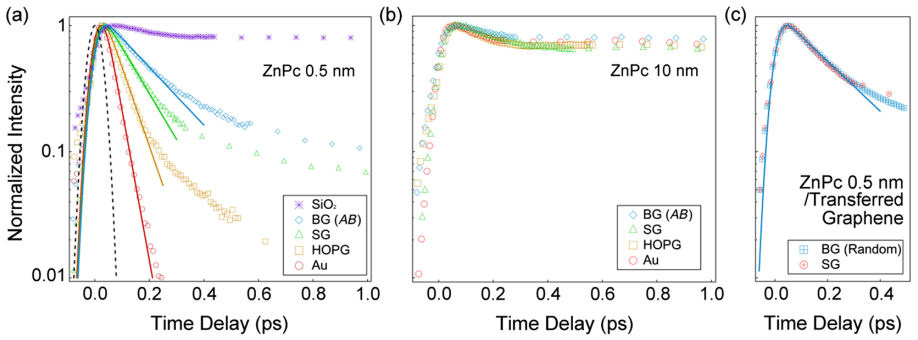

FIG. 4 The intensity of the S_1 state as a function of time for the (a) 0.5-nm samples and (b) 10-nm samples. For the 0.5-nm samples, the intensity decay is attributed to CT to the substrates. The initial CT rate is fitted with an exponential function convoluted with the instrumental response function (dashed line). The fits are shown as solid lines. The results for 10-nm samples represent the intrinsic S_1 dynamics of the ZnPc film. (c) The CT dynamics for 0.5 nm ZnPc deposited on transferred graphene. "*AB*" in the legend represents *AB*-stacked BG, while "Random" represents randomly stacked BG.

to metals is reported to have a transfer time in the range of 10–50 fs [40,60], which is comparable to our CT rate for Au. For interfaces dominated by π-orbital coupling, e.g., CT at organic-organic interfaces [49,50,54,55,61], the CT times are around 100 fs, which can be compared to our CT rate for graphene. After the first few hundred femtoseconds, CT becomes progressively slower. This is likely to be caused by electron relaxing to lower-energy traps at the interface, which impedes further CT. Therefore, it is critical to optimize the initial CT rate to avoid electron trapping at the interface. The S_1 intensity as a function of time for the 10-nm samples is shown in Fig. 4(b). The intensity decreases at a much slower rate, and the dynamics is independent of substrates. This result is expected, since it represents the intrinsic dynamics of ZnPc films.

Interestingly, the CT rate to *AB*-stacked BG is slower than the rates to both SG and HOPG instead of being in between the two rates. For comparison, 2PPE experiments are also done on graphene transferred to SiO_2 by using standard solution processes. In the transferred BG samples, since the two layers are transferred successively, they are misoriented and have a random-stacking relationship. Figure 4(c) shows the CT dynamics for ZnPc grown on transferred SG and BG. The initial CT rate is almost the same for the transferred SG and BG samples. Both curves can be fitted with an exponential decay with a time constant of 220 fs (solid line). Therefore, the anomalously slow CT rate in BG compared to SG is observed only when the BG is *AB* stacked, where the two graphene layers are coupled electronically to each other. We also note that CT to transferred graphene is slower compared to direct-grown graphene. For transferred graphene, it is known that a small amount of polymethyl methacrylate (PMMA) remains on the surface after the transfer [62]. For ZnPc molecules deposited on the residual PMMA, CT to graphene is likely to be slowed. Since our laser pulse samples a relatively large area (beam diameter about 0.8 mm), the average CT rate becomes apparently slower for the transferred graphene.

C. Charge-transfer model

The slower CT observed in BG compared to SG cannot be explained by traps, since the intensity ratio of the *D* and *G* peak in the Raman spectrum is small and similar for SG and BG [Fig. 1(a)], which indicates a comparable defect density. On the other hand, the results can be explained by considering the electronic band structure. In the nonadiabatic limit, the CT rate k_{CT} from an electron donor to an acceptor can be described by [63,64]

$$k_{CT} = \frac{2\pi}{\hbar}\sum_a |V_{da}|^2 F_{da}. \quad (1)$$

Here, V_{da} is the electronic coupling strength between the donor and acceptor, the index a represents all available acceptor states, and F_{da} is the Franck-Condon factor. In our case, since the acceptor (the conduction band of the substrate) has a continuum of states, one can generally find an acceptor level that has a barrierless transition [63]. This agrees with our observation that the CT rate is nearly the same at 150 K and at 300 K [35]. The acceptor state that allows a barrierless transition dominates CT and should locate energetically between the S_1 state of ZnPc and E_F [Fig. 2(b)]. Therefore, the transfer rate k_{CT} is proportional to the DOS of the substrate near E_F. Compared to graphene, bulk conductors usually have a much larger DOS near E_F. This agrees with our observation that CT to graphite and Au is faster than that to SG and BG.

To understand the difference between SG and BG, we need to consider their band structure. The band structure of SG and BG is well studied [65], which is reproduced here by using a tight-binding model. In our model, only the in-plane nearest-neighbor interaction and the *A*-*A* site interlayer coupling are considered. The coupling constant used for intra- and inter-layer coupling is −2.97 and 0.4 eV, respectively [66]. The band structure and the probability amplitudes of the eigenstates can be calculated by using the procedure outlined in Refs. [65,66]. The band structure

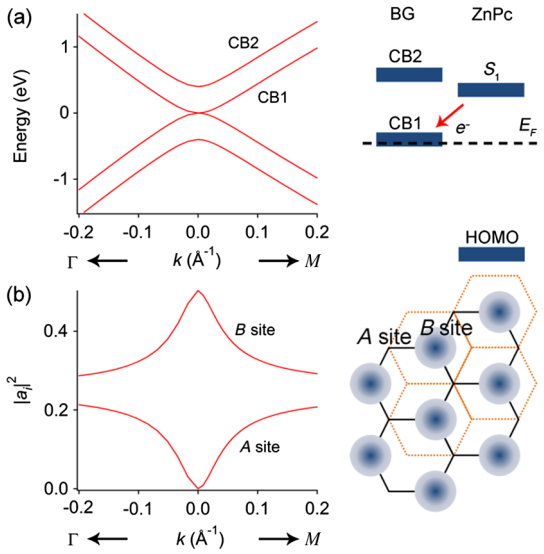

FIG. 5 (a) Electronic band structure of BG calculated by using a tight-binding model. The schematic on the right shows the energy alignment at the interface. (b) The electron probability amplitude at *A* and *B* sites for the CB1 band of BG. Near the *K* point, only *B* sites are occupied. The figure on the right shows the crystal structure of BG. The top and bottom layers are shown by black and orange lines, respectively. On the top layers, only *B* sites are occupied (blue shaded regions).

of BG is shown in Fig. 5(a). Note that one of the bands [CB2 in Fig. 5(a)] in BG is located at about 0.4 eV above E_F, which is slightly above the S_1 state. Energetically, the S_1 band only slightly overlaps with the bottom of the CB2 band. In addition, a small excess energy (approximately 0.1 eV) is often needed to facilitate CT in organic molecules because of nuclear reorganization. Taking these two factors into account, CB2 should be a much slower CT channel as compared to CB1. Here, we assume that CB1 dominates the CT for *AB*-stacked BG. Nevertheless, since one additional band is present in BG as compared to SG, the total CT rate to BG should still be increased by CB2 even though its contribution would be very small. Therefore, the DOS argument cannot explain the slower CT observed for *AB*-stacked BG. In order to explain the experimental results, we note that the CT rate also depends on the electronic coupling term V_{da} in Eq. (1), which depends on the wave function overlapping between the donor and acceptor states.

To this end, the wave function for the conduction band near E_F for SG and BG is determined. In a typical tight-binding model, the wave function can be written as

$$\Psi(k) = \sum_i a_i(k)\varphi_i. \tag{2}$$

In this equation, φ_i is the atomic orbital at site i, a_i is the probability amplitude, and the summation is done over all atoms in the basis. In SG, the magnitudes of a_i for *A* and *B* sites are always equal ($|a_A|^2 = |a_B|^2 = 0.5$). Hence, electrons occupy both the *A* and *B* sites [65]. Figure 5(b) shows $|a_i|^2$ for the *A* and *B* sites in BG. Only results for the CB1 band are shown. In contrast to SG, the probability amplitude at the *A* site vanishes near the *K* point; i.e., electrons occupy the *B* sites only [inset in Fig. 5(b)] [65]. Half of the sites in the layer that is in direct contact with the molecules have a zero electron density. Indeed, the other half of the probability density is located at the second layer. As a result, compared to SG, the wave function overlapping between the molecules and graphene in BG should be significantly weakened, especially since the wave function of the molecular state is rather localized. This leads to a smaller V_{da}. In summary, CT to CB1 becomes slower because of poor wave-function overlapping, while the contribution from CB2 to the overall CT rate is expected to be small, because it is located at an unfavorable energy position. As a result, the overall CT rate to BG becomes smaller as compared to SG. Note that this argument is valid only when the two graphene layers have a well-defined stacking relationship. Therefore, the anomalous CT rate is observed only in *AB*-stacked BG [Fig. 4(a)] but not in the transferred BG [Fig. 4(c)].

IV. CONCLUSION

Our results have several interesting implications to CT in systems where the donor state locates slightly above the conduction band minimum of graphene. First, for trilayer graphene with an *ABA* stacking, the CT rate should increase as compared to that in BG, because the additional conduction band introduced by the third layer is located near E_F (i.e., this band is expected to participate in CT). For each subsequent even (odd) layer added to the stack, the new band is locating away from (near to) E_F [65]. As a result, based on the above argument, the magnitude of the CT rate is expected to oscillate with the increase in the layer number until it converges to that for graphite. On the other hand, for trilayer graphene with an *ABC* stacking, the CT rate would be even smaller than that of *AB*-stacked bilayer graphene. This is because the new band introduced by the new layer is located away from E_F [67]. For the band located near E_F, the wave function is spread across three layers instead of two, which would further decrease the extent of wave-function overlapping with the molecular orbital. Finally, the present model is generic without considering the details of the molecular state. Therefore, the same conclusion can be generalized to the interaction between graphene and other organic semiconductors. In conclusion, the CT rate at the graphene–organic-semiconductor interface can be controlled via the total number of graphene layers and their stacking relationships, which provides a design strategy for optoelectronic devices using graphene as a conductor.

ACKNOWLEDGMENTS

This work is primarily supported by U.S. National Science Foundation, Grant No. DMR-1351716. W. L. C. also acknowledges the startup fund provided by University of Kansas. J. W. acknowledges support from ARO Contract No. W911NF-12-1-0412, NSF Contracts No. NSF-DMR-1105986, No. NSF-DMR-1508494 and No. NSF-EPSCoR-0903806, and matching support from the State of Kansas through Kansas Technology Enterprise Corporation.

[1] A. Pospischil, M. M. Furchi, and T. Mueller, Solar-energy conversion and light emission in an atomic monolayer p-n diode, Nat. Nanotechnol. **9**, 257 (2014).

[2] B. W. H. Baugher, H. O. H. Churchill, Y. Yang, and P. Jarillo-Herrero, Optoelectronic devices based on electrically tunable p-n diodes in a monolayer dichalcogenide, Nat. Nanotechnol. **9**, 262 (2014).

[3] J. S. Ross, P. Klement, A. M. Jones, N. J. Ghimire, J. Yan, D. G. Mandrus, T. Taniguchi, K. Watanabe, K. Kitamura, W. Yao, D. H. Cobden, and X. Xu, Electrically tunable excitonic light-emitting diodes based on monolayer WSe_2 p-n junctions, Nat. Nanotechnol. **9**, 268 (2014).

[4] C.-H. Liu, Y.-C. Chang, T. B. Norris, and Z. Zhong, Graphene photodetectors with ultra-broadband and high responsivity at room temperature, Nat. Nanotechnol. **9**, 273 (2014).

[5] F. Bonaccorso, L. Colombo, G. Yu, M. Stoller, V. Tozzini, A. C. Ferrari, R. S. Ruoff, and V. Pellegrini, Graphene, related two-dimensional crystals, and hybrid systems for energy conversion and storage, Science **347**, 1246501 (2015).

[6] G. Konstantatos, M. Badioli, L. Gaudreau, J. Osmond, M. Bernechea, F. P. G. de Arquer, F. Gatti, and F. H. Koppens, Hybrid graphene-quantum dot phototransistors with ultrahigh gain, Nat. Nanotechnol. **7**, 363 (2012).

[7] H. Park, P. R. Brown, V. Bulović, and J. Kong, Graphene as transparent conducting electrodes in organic photovoltaics: Studies in graphene morphology, hole transporting layers, and counter electrodes, Nano Lett. **12**, 133 (2012).

[8] L. Gomez De Arco, Y. Zhang, C. W. Schlenker, K. Ryu, M. E. Thompson, and C. Zhou, Continuous, highly flexible, and transparent graphene films by chemical vapor deposition for organic photovoltaics, ACS Nano **4**, 2865 (2010).

[9] Q. Liu, Z. Liu, X. Zhang, L. Yang, N. Zhang, G. Pan, S. Yin, Y. Chen, and J. Wei, Polymer photovoltaic cells based on solution-processable graphene and P3HT, Adv. Funct. Mater. **19**, 894 (2009).

[10] Y. Wang, S. W. Tong, X. F. Xu, B. özyilmaz, and K. P. Loh, Interface engineering of layer-by-layer stacked graphene anodes for high-performance organic solar cells, Adv. Mater. **23**, 1514 (2011).

[11] Z. Liu, K. Parvez, R. Li, R. Dong, X. Feng, and K. Müllen, Transparent conductive electrodes from graphene/PEDOT: PSS hybrid inks for ultrathin organic photodetectors, Adv. Mater. **27**, 669 (2015).

[12] W. C. Tan, W. H. Shih, and Y. F. Chen, A highly sensitive graphene-organic hybrid photodetector with a piezoelectric substrate, Adv. Funct. Mater. **24**, 6818 (2014).

[13] N. Li, S. Oida, G. S. Tulevski, S.-J. Han, J. B. Hannon, D. K. Sadana, and T.-C. Chen, Efficient and bright organic light-emitting diodes on single-layer graphene electrodes, Nat. Commun. **4**, 2294 (2013).

[14] J. Meyer, P. R. Kidambi, B. C. Bayer, C. Weijtens, A. Kuhn, A. Centeno, A. Pesquera, A. Zurutuza, J. Robertson, and S. Hofmann, Metal oxide induced charge transfer doping and band alignment of graphene electrodes for efficient organic light emitting diodes, Sci. Rep. **4**, 5380 (2014).

[15] M. He, J. Jung, F. Qiu, and Z. Lin, Graphene-based transparent flexible electrodes for polymer solar cells, J. Mater. Chem. **22**, 24254 (2012).

[16] W. Chen, S. Chen, D. C. Qi, X. Y. Gao, and A. T. S. Wee, Surface transfer p-type doping of epitaxial graphene, J. Am. Chem. Soc. **129**, 10418 (2007).

[17] G. Hong, Q.-H. Wu, J. Ren, C. Wang, W. Zhang, and S.-T. Lee, Recent progress in organic molecule/graphene interfaces, Nano Today **8**, 388 (2013).

[18] M.-E. Ragoussi, G. Katsukis, A. Roth, J. Malig, G. de la Torre, D. M. Guldi, and T. Torres, Electron-donating behavior of few-layer graphene in covalent ensembles with electron-accepting phthalocyanines, J. Am. Chem. Soc. **136**, 4593 (2014).

[19] N. Karousis, J. Ortiz, K. Ohkubo, T. Hasobe, S. Fukuzumi, A. n. Sastre-Santos, and N. Tagmatarchis, Zinc phthalocyanine–graphene hybrid material for energy conversion: Synthesis, characterization, photophysics, and photoelectrochemical cell preparation, J. Phys. Chem. C **116**, 20564 (2012).

[20] H. S. S. Ramakrishna Matte, K. S. Subrahmanyam, K. Venkata Rao, S. J. George, and C. N. R. Rao, Quenching of fluorescence of aromatic molecules by graphene due to electron transfer, Chem. Phys. Lett. **506**, 260 (2011).

[21] F. Prins, A. J. Goodman, and W. A. Tisdale, Reduced dielectric screening and enhanced energy transfer in single-and few-layer MoS_2, Nano Lett. **14**, 6087 (2014).

[22] W.-T. Hsu, Z.-A. Zhao, L.-J. Li, C.-H. Chen, M.-H. Chiu, P.-S. Chang, Y.-C. Chou, and W.-H. Chang, Second harmonic generation from artificially stacked transition metal dichalcogenide twisted bilayers, ACS Nano **8**, 2951 (2014).

[23] N. Kumar, S. Najmaei, Q. Cui, F. Ceballos, P. M. Ajayan, J. Lou, and H. Zhao, Second harmonic microscopy of monolayer MoS_2, Phys. Rev. B **87**, 161403 (2013).

[24] S. Hu, M. Lozada-Hidalgo, F. C. Wang, A. Mishchenko, F. Schedin, R. R. Nair, E. W. Hill, D. W. Boukhvalov, M. I. Katsnelson, and R. A. W. Dryfe, Proton transport through one-atom-thick crystals, Nature (London) **516**, 227 (2014).

[25] X. Qian, J. Liu, L. Fu, and J. Li, Quantum spin Hall effect in two-dimensional transition metal dichalcogenides, Science **346**, 1344 (2014).

[26] B. Hunt, J. D. Sanchez-Yamagishi, A. F. Young, M. Yankowitz, B. J. LeRoy, K. Watanabe, T. Taniguchi, P. Moon, M. Koshino, P. Jarillo-Herrero, and R. C. Ashoori, Massive Dirac fermions and Hofstadter butterfly in a van der Waals heterostructure, Science **340**, 1427 (2013).

[27] Z. H. Ni, Y. Y. Wang, T. Yu, and Z. X. Shen, Raman spectroscopy and imaging of graphene, Nano Res. **1**, 273 (2008).
[28] A. Gupta, G. Chen, P. Joshi, S. Tadigadapa, and P. C. Eklund, Raman scattering from high-frequency phonons in supported n-graphene layer films, Nano Lett. **6**, 2667 (2006).
[29] A. C. Ferrari, J. C. Meyer, V. Scardaci, C. Casiraghi, M. Lazzeri, F. Mauri, S. Piscanec, D. Jiang, K. S. Novoselov, S. Roth, and A. K. Geim, Raman Spectrum of Graphene and Graphene Layers, Phys. Rev. Lett. **97**, 187401 (2006).
[30] W. Fang, A. L. Hsu, R. Caudillo, Y. Song, A. G. Birdwell, E. Zakar, M. Kalbac, M. Dubey, T. Palacios, M. S. Dresselhaus, P. T. Araujo, and J. Kong, Rapid identification of stacking orientation in isotopically labeled chemical-vapor grown bilayer graphene by Raman spectroscopy, Nano Lett. **13**, 1541 (2013).
[31] K. Yan, H. L. Peng, Y. Zhou, H. Li, and Z. F. Liu, Formation of bilayer bernal graphene: Layer-by-layer epitaxy via chemical vapor deposition, Nano Lett. **11**, 1106 (2011).
[32] W. Liu, S. Kraemer, D. Sarkar, H. Li, P. M. Ajayan, and K. Banerjeet, Controllable and rapid synthesis of high-quality and large-area bernal stacked bilayer graphene using chemical vapor deposition, Chem. Mater. **26**, 907 (2014).
[33] W. Liu, H. Li, C. Xu, Y. Khatami, and K. Banerjee, Synthesis of high-quality monolayer and bilayer graphene on copper using chemical vapor deposition, Carbon **49**, 4122 (2011).
[34] Q. Liu, Y. Gong, T. Wang, W.-L. Chan, and J. Wu, Metal-catalyst-free and controllable synthesis of monolayer, bilayer and few-layer graphene on silicon dioxide by chemical vapor deposition (to be published).
[35] See Supplemental Material at http://link.aps.org/supplemental/10.1103/PhysRevApplied.4.014016 for details of AFM, UPS, and 2PPE analysis.
[36] G. Giovannetti, P. A. Khomyakov, G. Brocks, V. M. Karpan, J. Van den Brink, and P. J. Kelly, Doping graphene with metal contacts, Phys. Rev. Lett. **101**, 026803 (2008).
[37] X. Li, Y. Zhu, W. Cai, M. Borysiak, B. Han, D. Chen, R. D. Piner, L. Colombo, and R. S. Ruoff, Transfer of large-area graphene films for high-performance transparent conductive electrodes, Nano Lett. **9**, 4359 (2009).
[38] S. Latil, V. Meunier, and L. Henrard, Massless fermions in multilayer graphitic systems with misoriented layers: Ab initio calculations and experimental fingerprints, Phys. Rev. B **76**, 201402 (2007).
[39] T. Wang and W.-L. Chan, Dynamical localization limiting the coherent transport range of excitons in organic crystals, J. Phys. Chem. Lett. **5**, 1812 (2014).
[40] E. Varene, L. Bogner, C. Bronner, and P. Tegeder, Ultrafast Exciton Population, Relaxation, and Decay Dynamics in Thin Oligothiophene Films, Phys. Rev. Lett. **109**, 207601 (2012).
[41] W. Gao and A. Kahn, Electronic structure and current injection in zinc phthalocyanine doped with tetrafluorotetracyanoquinodimethane: Interface versus bulk effects, Org. Electron. **3**, 53 (2002).
[42] C. H. Schwalb, S. Sachs, M. Marks, A. Schöll, F. Reinert, E. Umbach, and U. Höfer, Electron Lifetime in a Shockley-Type Metal-Organic Interface State, Phys. Rev. Lett. **101**, 146801 (2008).
[43] B. W. Caplins, D. E. Suich, A. J. Shearer, and C. B. Harris, Metal/phthalocyanine hybrid interface states on Ag (111), J. Phys. Chem. Lett. **5**, 1679 (2014).
[44] B. W. Caplins, A. J. Shearer, D. E. Suich, E. A. Muller, and C. B. Harris, Measuring the electronic corrugation at the metal/organic interface, Phys. Rev. B **89**, 155422 (2014).
[45] T. Wang, C. Caraiani, G. W. Burg, and W.-L. Chan, From two-dimensional electron gas to localized charge: Dynamics of polaron formation in organic semiconductors, Phys. Rev. B **91**, 041201 (2015).
[46] M. Scardamaglia, S. Lisi, S. Lizzit, A. Baraldi, R. Larciprete, C. Mariani, and M. G. Betti, Graphene-induced substrate decoupling and ideal doping of a self-assembled iron-phthalocyanine single layer, J. Phys. Chem. C **117**, 3019 (2013).
[47] W. Dou, S. Huang, R. Q. Zhang, and C. S. Lee, Molecule–substrate interaction channels of metal-phthalocyanines on graphene on Ni (111) surface, J. Chem. Phys. **134**, 094705 (2011).
[48] M. P. Seah and W. A. Dench, Quantitative electron spectroscopy of surfaces: A standard data base for electron inelastic mean free paths in solids, Surf. Interface Anal. **1**, 46 (1979).
[49] W.-L. Chan, J. R. Tritsch, and X.-Y. Zhu, Harvesting singlet fission for solar energy conversion: One- versus two-electron transfer from the quantum mechanical superposition, J. Am. Chem. Soc. **134**, 18295 (2012).
[50] W.-L. Chan, M. Ligges, A. Jailaubekov, L. Kaake, L. Miaja-Avila, and X.-Y. Zhu, Observing the multiexciton state in singlet fission and ensuing ultrafast multielectron transfer, Science **334**, 1541 (2011).
[51] S. Hüfner, *Photoelectron Spectroscopy: Principles and Applications* (Springer-Verlag, Berlin, 2003).
[52] J. C. Johannsen, S. Ulstrup, F. Cilento, A. Crepaldi, M. Zacchigna, C. Cacho, I. C. E. Turcu, E. Springate, F. Fromm, and C. Raidel, Direct View of Hot Carrier Dynamics in Graphene, Phys. Rev. Lett. **111**, 027403 (2013).
[53] D. Nobis, M. Potenz, D. Niesner, and T. Fauster, Image-potential states of graphene on noble-metal surfaces, Phys. Rev. B **88**, 195435 (2013).
[54] A. E. Jailaubekov, A. P. Willard, J. R. Tritsch, W.-L. Chan, N. Sai, R. Gearba, L. G. Kaake, K. J. Williams, K. Leung, and P. J. Rossky, Hot charge-transfer excitons set the time limit for charge separation at donor/acceptor interfaces in organic photovoltaics, Nat. Mater. **12**, 66 (2013).
[55] B. Kraabel, C. H. Lee, D. McBranch, D. Moses, N. S. Sariciftci, and A. J. Heeger, Ultrafast photoinduced electron transfer in conducting polymer-buckminsterfullerene composites, Chem. Phys. Lett. **213**, 389 (1993).
[56] W. A. Tisdale, K. J. Williams, B. A. Timp, D. J. Norris, E. S. Aydil, and X.-Y. Zhu, Hot-electron transfer from semiconductor nanocrystals, Science **328**, 1543 (2010).
[57] N. A. Anderson and T. Lian, Ultrafast electron transfer at the molecule-semiconductor nanoparticle interface, Annu. Rev. Phys. Chem. **56**, 491 (2005).
[58] L. Gundlach, R. Ernstorfer, and F. Willig, Ultrafast interfacial electron transfer from the excited state of anchored

molecules into a semiconductor, Prog. Surf. Sci. **82**, 355 (2007).

[59] R. R. Lunt, N. C. Giebink, A. A. Belak, J. B. Benziger, and S. R. Forrest, Exciton diffusion lengths of organic semiconductor thin films measured by spectrally resolved photoluminescence quenching, J. Appl. Phys. **105**, 053711 (2009).

[60] G. Dutton, D. P. Quinn, C. D. Lindstrom, and X.-Y. Zhu, Exciton dynamics at molecule-metal interfaces: C_{60}/Au (111), Phys. Rev. B **72**, 045441 (2005).

[61] G. J. Dutton, W. Jin, J. E. Reutt-Robey, and S. W. Robey, Ultrafast charge-transfer processes at an oriented phthalocyanine/C_{60} interface, Phys. Rev. B **82**, 073407 (2010).

[62] A. Pirkle, J. Chan, A. Venugopal, D. Hinojos, C. W. Magnuson, S. McDonnell, L. Colombo, E. M. Vogel, R. S. Ruoff, and R. M. Wallace, The effect of chemical residues on the physical and electrical properties of chemical vapor deposited graphene transferred to SiO_2, Appl. Phys. Lett. **99**, 122108 (2011).

[63] J. Nieto-Pescador, B. Abraham, and L. Gundlach, Photoinduced ultrafast heterogeneous electron transfer at molecule-semiconductor interfaces, J. Phys. Chem. Lett. **5**, 3498 (2014).

[64] V. May and O. Kühn, *Charge and Energy Transfer Dynamics in Molecular Systems* (Wiley, New York, 2008).

[65] B. Partoens and F. M. Peeters, From graphene to graphite: Electronic structure around the K point, Phys. Rev. B **74**, 075404 (2006).

[66] M. I. Katsnelson, *Graphene: Carbon in Two Dimensions* (Cambridge University Press, Cambridge, England, 2012).

[67] F. Zhang, B. Sahu, H. Min, and A. H. MacDonald, Band structure of ABC-stacked graphene trilayers, Phys. Rev. B **82**, 035409 (2010).